nature biotechnology

Supplementary information https://doi.org/10.1038/s41587-026-03294-y

Engineered genomic attachment sites for site-specific recombinases enable high-efficiency integration in plants and human cells

In the format provided by the authors and unedited

Supplementary Information

Table of contents

Supplemental Figures

Supplemental Fig. 1 The 3D protein structure of Bxb1 predicted by AlphaFold2 and 5 split domains. SD, the N-terminal catalytic domain. RD, the recombination domain. ZD, zinc-binding domain. CC, coil-coiled domain. TD, tail domain.

Supplemental Fig. 2 Parallel comparison of integration efficiency among diverse recombinases and variants in rice. a. Schematic diagram to parallelly compare the integration efficiency among diverse recombinases and variants at *GSH1* site in rice protoplasts. **b.** The prime editing and integration efficiency. Data show the mean ± s.d. of three biological replicates. Statistical significance was determined using one-way ANOVA followed by Dunnett's multiple comparisons test.

Supplemental Fig. 3 The *attB(V111)* insertion efficiency upstream of *OsEPSPS* site of different dual-epegRNA combinations in rice protoplasts. Data show the mean ± s.d of two biological replicates.

Supplemental Fig. 4 The central *GT* dinucleotides in *att* is orthogonal to *GA* in tobacco leaves. Fold-change in inversion activity relative to *att-GT* sites. Data show the mean ± s.d. Each dot represents an independent biological replicate.

Supplemental Fig. 5 Sanger sequencing traces of the *attL(V111)* and *attR(V111)* after integration of *OsEPSPS* cassette upstream of *OsEPSPS* site in rice plant. Primers used are listed in Supplemental Table.

Supplemental Fig. 6 Alignment of Oxford Nanopore (ONT) reads spanning sites identified by NGS.

Supplemental Fig. 7 Sanger sequencing traces of the *attL* and *attR* after integration at *TRAC* site. Primers used are listed in Supplemental Table.

Supplemental Fig. 8 Parallel comparison of integration efficiency among diverse recombinases and variants in HEK293T cells. a. Schematic diagram to parallelly compare the integration efficiency among diverse recombinases and variants at *TRAC* site in HEK293T cells. **b.** The prime editing and integration efficiency. Data show the mean ± s.d. of three biological replicates. Statistical significance was determined using one-way ANOVA followed by Dunnett's multiple comparisons test.

Supplemental Fig. 9 *attB* insertion efficiency and the integration efficiency of Bxb1 variants at *TRAC* site. a. *attB* insertion efficiency at *TRAC* site. **b.** The donor integration efficiency. Data show the mean ± s.d. Each dot represents an individual biological replicate.

Supplemental Table 1.

Supplemental Fig. 1 The 3D protein structure of Bxb1 predicted by AlphaFold2 and 5 split domains. SD, the N-terminal catalytic domain. RD, the recombination domain. ZD, zinc-binding domain. CC, coil-coiled domain. TD, tail domain. AA: amino acid.

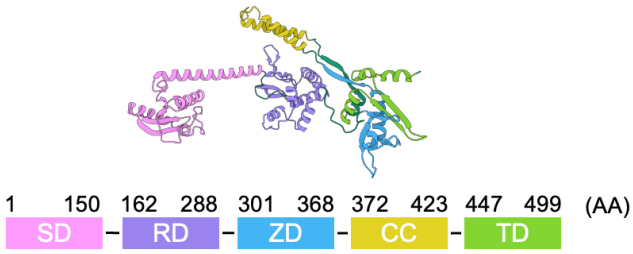

Supplemental Fig. 2 Parallel comparison of integration efficiency among diverse recombinases and variants in rice. a. Schematic diagram to parallelly compare the integration efficiency among diverse recombinases and variants at *GSH1* site in rice protoplasts. **b.** The prime editing and integration efficiency. Data show the mean ± s.d. of three biological replicates. Statistical significance was determined using one-way ANOVA followed by Dunnett's multiple comparisons test.

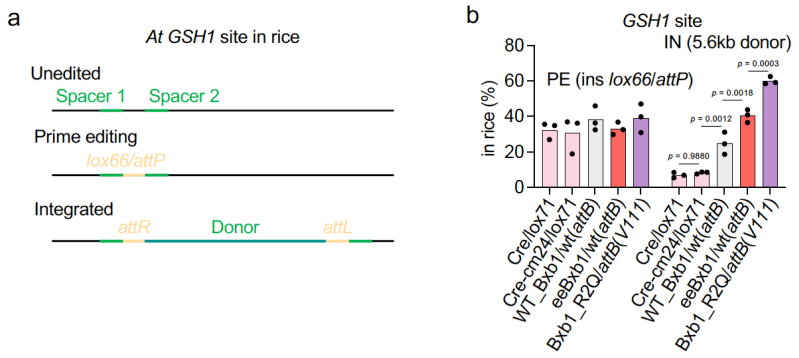

Supplemental Fig. 3 The *attB(V111)* insertion efficiency upstream of *OsEPSPS* site of different dual-epegRNA combinations in rice protoplasts. Data show the mean ± s.d of two biological replicates.

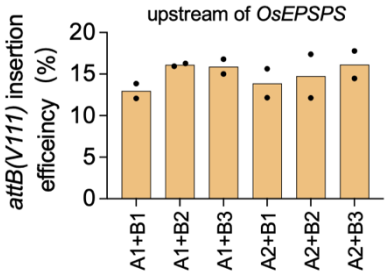

Supplemental Fig. 4 The central *GT* dinucleotides in *att* is orthogonal to *GA* in tobacco leaves. Fold-change in inversion activity relative to *att-GT* sites. Data show the mean ± s.d. Each dot represents an independent biological replicate.

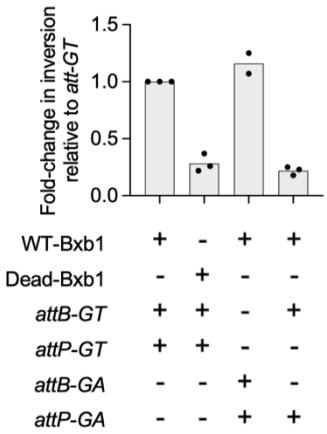

Supplemental Fig. 5 Sanger sequencing traces of the *attL(V111)* and *attR(V111)* after integration of *OsEPSPS* cassette upstream of *OsEPSPS* site in rice plant. Primers used are listed in Supplemental Table 1.

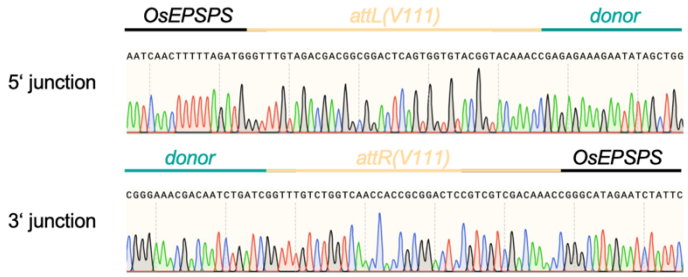

Supplemental Fig. 6 Alignment of Oxford Nanopore (ONT) reads spanning sites identified by NGS.

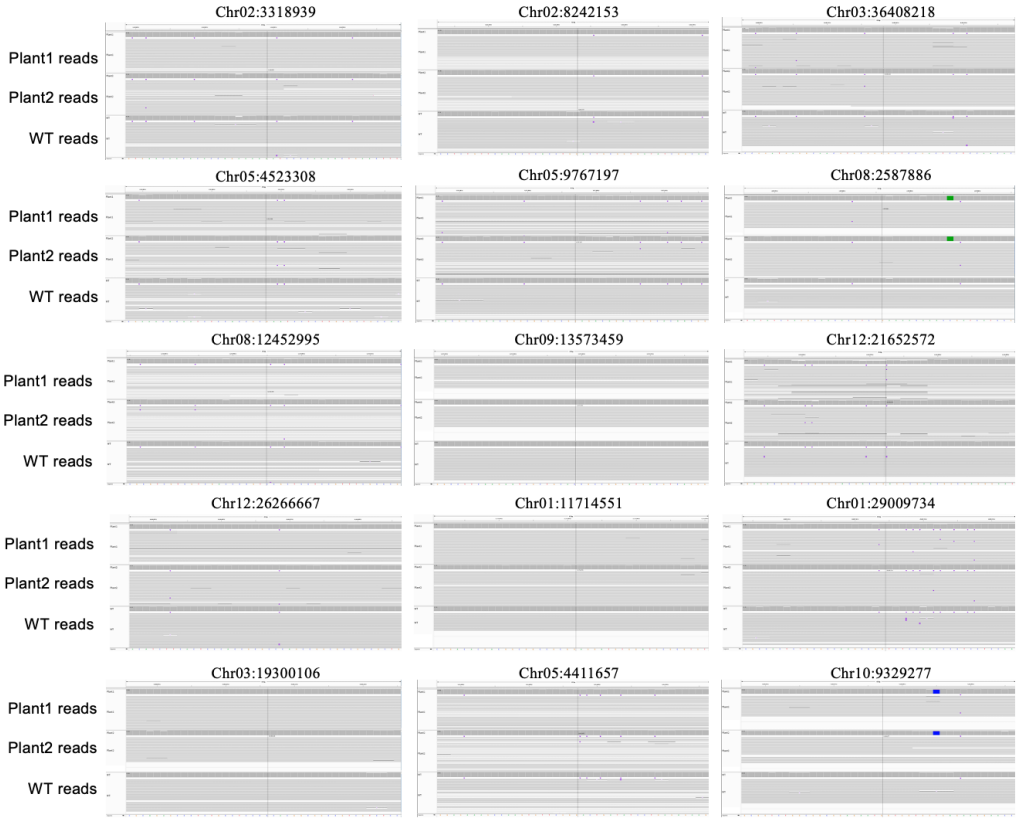

Supplemental Fig. 7 Sanger sequencing traces of the *attL* and *attR* after integration at *TRAC* site. Primers used are listed in Supplemental Table 1.

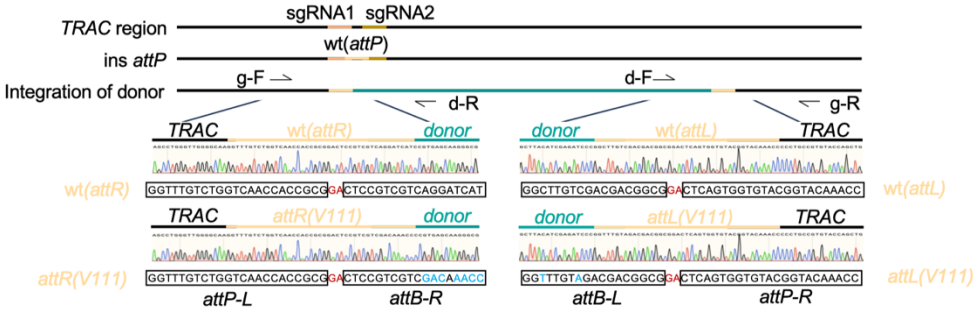

Supplemental Fig. 8 Parallel comparison of integration efficiency among diverse recombinases and variants in HEK293T cells. a. Schematic diagram to parallelly compare the integration efficiency among diverse recombinases and variants at *TRAC* site in HEK293T cells. **b.** The prime editing and integration efficiency. Data show the mean ± s.d. of three biological replicates. Statistical significance was determined using one-way ANOVA followed by Dunnett's multiple comparisons test.

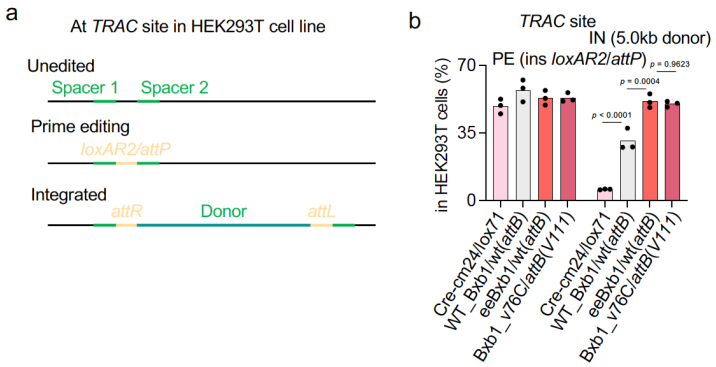

Supplemental Fig. 9 *attB* insertion efficiency and the integration efficiency of Bxb1 variants at *TRAC* site. a. *attB* insertion efficiency at *TRAC* site. **b.** The donor integration efficiency. Data show the mean ± s.d. Each dot represents an individual biological replicate.

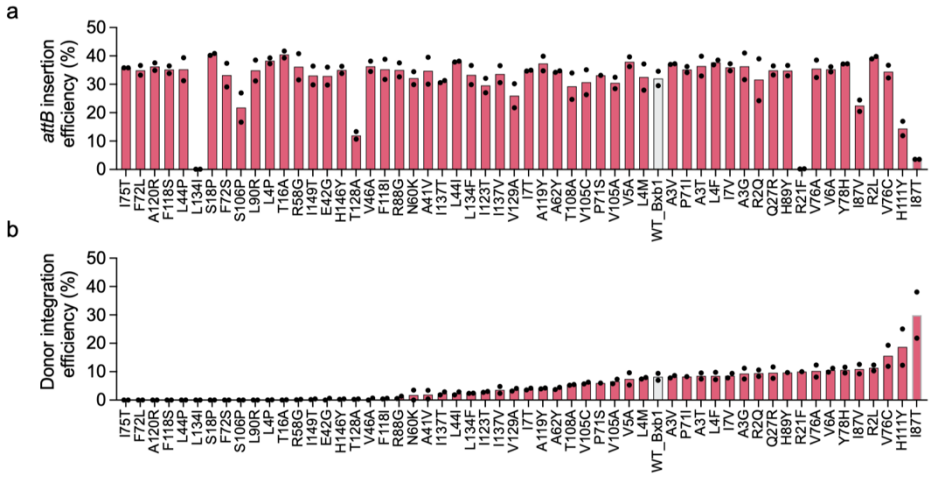

Supplemental Table 1. Provided as separate xlsx. file